A version of this chapter has been published in Am J Respir Cell Mol Biol, May, 2008

> *"You must do things you think you cannot do"*
> *Eleanor Roosevelt*

Chapter 5. LSCM Lung Imaging

Abstract: Understanding the structure and function of alveoli in un-fixed fresh lungs and, better still, *in vivo,* is crucial for understanding the normal and diseased lung. To date, investigation of the lung at the alveolar level has been performed using histology, a static and destructive imaging approach. However, the lung is a highly dynamic organ not only in its underlying physiologic, molecular and biochemical processes, but also its important mechanical processes. New approaches are needed to investigate the lung in a dynamic fashion.

In the following chapter, two dynamic lung imaging techniques are introduced. The first is an *ex vivo* confocal microscopy technique that allows direct visualization of sub-pleural alveoli in fresh intact mouse lungs. The second is a flexible fiber optic based confocal microscopy system that allows imaging of alveoli in live breathing mouse lungs.

Using the confocal microscopy techniques detailed in this chapter, alveoli and surrounding structures are clearly resolved during dynamic events. Through empirical data obtained using this approach, a new theory on alveolar recruitment / de-recruitment is proposed.

5.1 Introduction

The primary role of the lung is respiration of oxygen into- and carbon dioxide out of- the bloodstream. The lungs contain millions of small gas exchange units called alveoli. Alveoli are small air pockets covered with a dense capillary network with only a single cell layer separating inhaled air and the circulating bloodstream. This unique structure allows for extremely efficient gas exchange. Currently, the most common method for investigating the structure of alveoli is through histology where tissue is excised, fixed, sectioned and stained for microscopic visualization as discussed in Chapter 2. However, there are numerous opportunities for processing artifacts to alter the inherent structure of the alveoli as they exist *in vivo*. Also, studying fixed tissue limits the visualization to an instantaneous moment in time when the tissue was removed and fixed. Such static imaging is informative in its own right, but is no comparison to dynamic imaging where structural and biochemical changes over time can be accurately assessed.

Repeated quantitative visualization at the alveolar level in unfixed breathing lung, without the overlying pleura partially obstructing the view, has yet to be accomplished and would be a significant contribution [170]. Furthermore, development of techniques for direct bedside monitoring of alveolar dynamics would be a major step forward in clinical ventilator management [171].

In the following chapter, two dynamic lung imaging techniques are introduced. The first is an *ex vivo* confocal microscopy technique that allows direct visualization of sub-pleural alveoli in fresh intact mouse lungs. The second is a flexible fiber optic based confocal microscopy system that allows imaging of alveoli in live, breathing mouse lungs.

In the first section, a novel phenomenon is observed when assessing the change in alveolar size during inflation and deflation using the *ex vivo* technique. Through automated quantification of the acquired images and analysis of the results, a new theory on alveolar recruitment and de-recruitment is proposed.

In the second section, a series of image acquisition, processing and analysis steps are developed to acquire high-resolution images of alveoli in live mice using the fiber optic based system. The *in vivo* imaging results confirm that direct dynamic visualization of alveoli and surrounding structures is possible. Furthermore, analysis of the alveolar area, size and number can be reliably performed using this imaging approach. Finally, a high-speed CBCM system is utilized to investigate whether the alveolar "popping" phenomenon occurs *in vivo*.

5.2 Ex Vivo Lung Imaging

5.2.1 Introduction

Mechanical changes in alveolar structure during respiration, also known as alveolar mechanics, have been widely discussed, yet no established unifying hypothesis exists. Much of the uncertainty has been due to the difficulties in documenting alveolar mechanics, given their small size and the large movement of the lung during breathing. Alveolar mechanics have largely been inferred from pulmonary function tests and static histopathology of one form or another, which although providing a better understanding of whole lung mechanics, are not specific [172]. To better understand alveolar based diseases and for further improvement of ventilator management, direct evidence regarding alveolar mechanics is required.

The process of recruitment and de-recruitment of alveoli has been controversially discussed with no unifying theory on its mechanism. There are several common hypotheses not restricted to: balloon-like expansion of alveoli, limited expansion of alveoli with major expansion in the airways and ducts, or continual recruitment and de-recruitment of alveoli [173].

Further advancement in techniques for investigation into alveolar mechanics is needed and ideally would occur *in vivo* with the alveoli visible in three-dimensions. The technology required to provide the spatial and temporal resolution to perform such a task is still in development.

There have been light-scattering techniques employed in studies by Butler et al, where the pattern of light backscattered by lung tissue below the pleura was used to calculate the size of respective airspaces in dynamic studies. This was a very elegant technique based on sound optics theory, but no visualization is performed, leaving open questions about the tissue under analysis [174-177].

The most recently proposed alternative for imaging sub-pleural alveolar structure is Fourier domain optical coherence tomography [178]. In their feasibility study, Popp et al. initially evaluated formalin fixed rabbit lung followed by isolated fresh lungs. Sub-pleural alveolar walls could be identified, but changes in individual alveoli could not be seen with certainty because of limitations in resolution and acquisition speed. No measurements were presented in this study. Also, tissue subtypes could not be discriminated due to the current technical limitations. Nevertheless, this method has great potential if improved upon and, in the future, may provide further valuable insight.

There have also been direct dynamic studies imaging the pleural surface aspect of alveoli using two-dimensional *in vivo* video microscopy techniques [14, 170, 179-184]. These studies evaluate the alveolar dimensions as seen through the overlying pleural surface with the expected lack of detailed morphology and measurement. These studies have been informative in describing novel behaviors of the alveolar structures, usually in the pig and rat lung. This methodology is limited to a superficial view of the alveoli through a glass plate suction-adhered to the pleura, leaving unanswered information regarding the underlying structures.

Recently, through such *in vivo* studies along with focused histological examination, there is a growing consensus suggesting alveoli are stable during normal lung tidal breathing, and changes in lung volume are the result of a greater number of open alveoli [185]. Smaldone et al. observed recruitment of smaller alveoli, [186] and in a later study involving histologic measurements of gerbil lungs fixed at various volumes, and Lum et al. concluded that lung volume change was the result of alveolar recruitment de-recruitment [187]. Escolar et al. has also demonstrated that lung volume change is largely due to the number of alveoli and further postulated that the hysterisis between the inflation and deflation limb commonly observed in P-V curves was the result of the number of open alveoli [188]. Concepts presented in these studies are increasingly gaining acceptance, but understanding the underlying mechanisms still requires further investigation.

Our prevailing hypothesis is that during early inspiration the alveolar size stays the same, with the initial volume change being absorbed by expansion of the airways and ducts, while alveolar size increase and recruitment occur during the final stages of inspiration. To partially test this hypothesis, we have used Laser Scanning Confocal Microscopy (LSCM) to quantitatively visualize sub-pleural alveoli of fresh mouse lungs through the full respiratory cycle.

5.2.2 Methods and Materials

5.2.2.1 Animal preparation

Animal experiments carried out in this study were approved by the University of Iowa Animal Care Committee. C56BL/6 mice (n=5)(Harlan) of 5-6 weeks in age, weighing 19-21 grams were initially sedated using 3-5% isofluorane, weighed, and anesthetized with an intra peritoneal (I.P.) injection of 87.5mg/kg ketamine and 12.5mg/kg xylazine. Following a negative pedal reflex, 50mg/kg of fluorescein was administered IP to provide a reasonable fluorescence tissue signal. Ten minutes was allowed for the uptake of fluorescein throughout the body, and the mouse was consequently euthanized through an overdose of 150mg/kg pentobarbital followed by transection of the abdominal aorta once respiration had ceased. A tracheotomy was performed via a mid-line incision on the trachea and insertion of a 20-gauge catheter, and the lungs were carefully excised. The intact lungs were placed into a custom made chamber (Figure 5.1) filled with Phosphate Buffer Saline (PBS). The lungs were connected via the tracheal catheter to a custom water column pressure controller. A single active inflation of the lungs through a tracheal pressure to 30 cmH_2O while immersed in PBS was completed to assess for punctures in the tissue. This inflation was maintained for approximately one second and then passively deflated to 0 cmH_2O pressure until the imaging routine had been initiated. In general, this time frame was 20 minutes.

5.2.2.2 Laser scanning confocal microscope

A Bio-Rad 1024 Radiance system using a 488nm Krypton-Argon laser was used for imaging in this study. Automated z sections were obtained on a 1024x1024 grid, with a pixel size of 1.2µm and section thickness of 5µm using a 10x Plan Fluor objective.

5.2.2.3 Ex vivo lung chamber

A custom chamber was developed for housing the lungs during image acquisition, Figure 5.1. The chamber contains an area for a mouse lung to bathe in PBS. The tracheal catheter is then connected to a tube that passes through the chamber parallel to the image plane, and a 45x50mm cover slip is mounted over the upper void of the chamber to water and air seal the chamber. The chamber provides stability during imaging, prevents the lung dehydrating when imaging under the LSCM, and reduces the effects of fluorescent quenching. The chamber is watertight and allows accurate tracking of the change in lung volume as it is inflated.

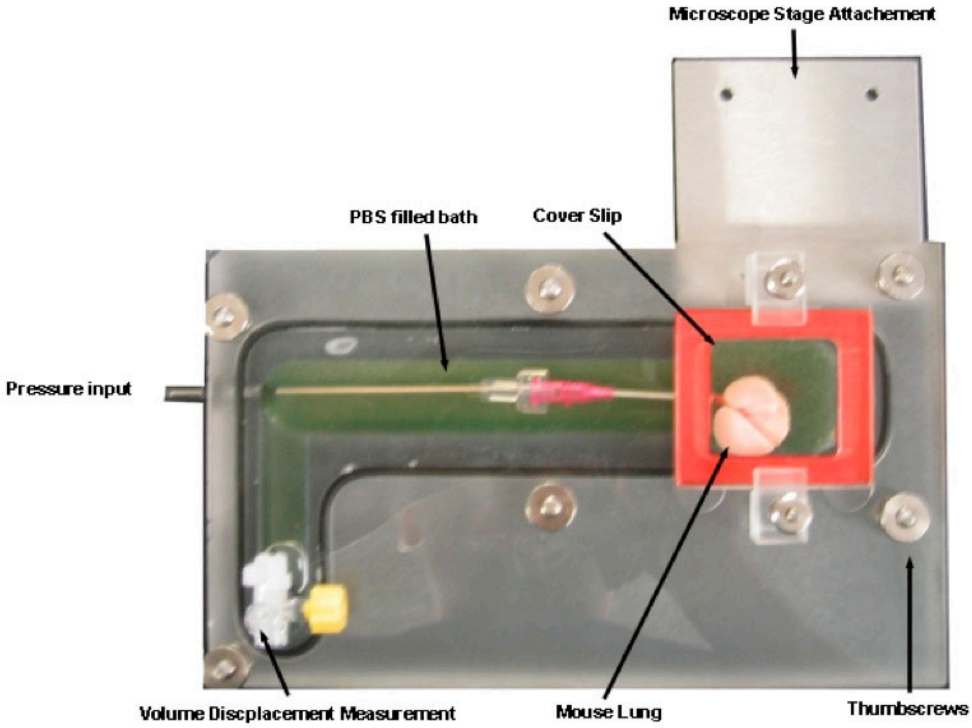

Figure 5.1: *Ex vivo* mouse lung imaging chamber, which is air and water tight to allow measurement of lung volume change.

5.2.2.4 Pressure controller

The catheter is connected to a custom water column pressure controller, which maintains a user defined pressure level within the lung. This system is made up of a piezo electric double pneumatic solenoid controlled using a proportional integrative derivative (PID) microcomputer, which can be set to any pressure between 0-50 cmH_2O. This system allows highly accurate and constant (iso) pressures with a tight tolerance to be fed and maintained through the entire imaging period. The microcomputer controller enables the accurate repeatability needed between studies. An Omega HHP680 electronic monometer (Omega Engineering, CT) is also connected between the tracheal tube and the controller in order to monitor the inline pressure.

5.2.2.5 Imaging routine

Lungs were inflated to the desired pressure levels sequentially (0, 5, 10, 15, 20, 25, 30 & 35 cmH_2O), and a 30 micron z series was acquired followed by a deflation and acquisition in the reverse stepwise manner. A schematic of the LSCM ex vivo mouse lung imaging setup is shown in Figure 5.2.

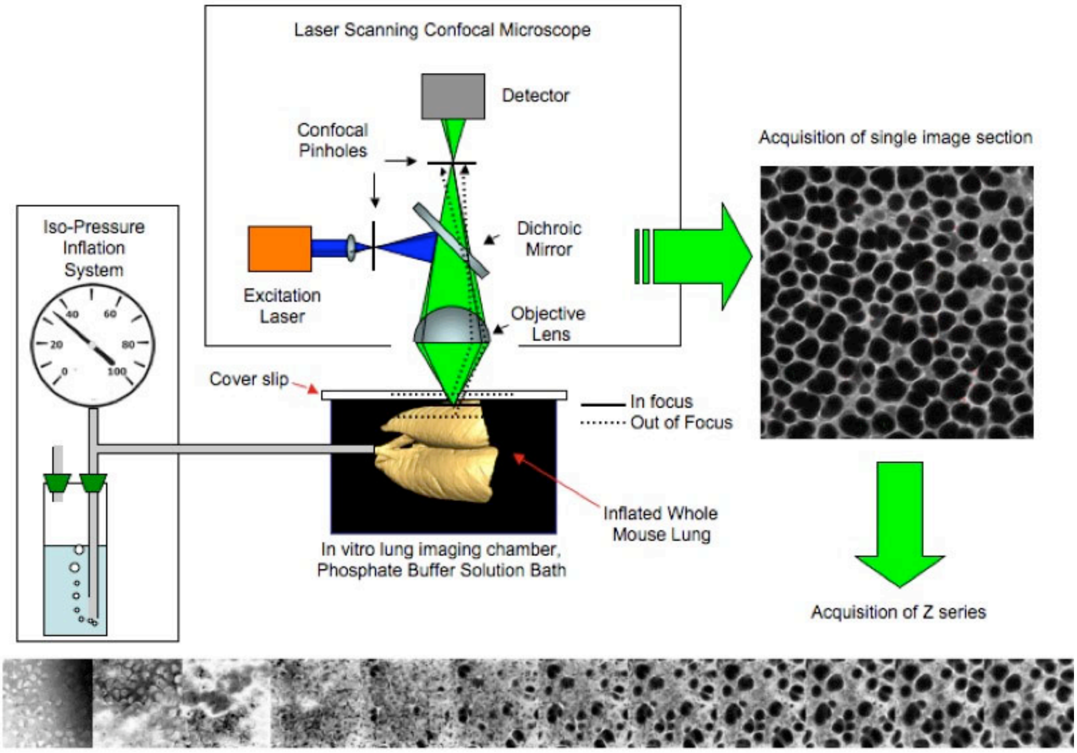

Figure 5.2: *Ex vivo* mouse lung imaging schematic, consists of a custom iso-pressure system for inflating the lung to the desired pressure, a commercial Bio-Rad laser scanning confocal microscope and a custom in vitro air and water tight lung imaging chamber.

5.2.2.6 Morphometric analysis

In this study, we calculate mean chord length (MCL) of the alveolar airspace and walls, along with alveolar airspace number using an automated custom application developed using Matlab (Mathworks, Natick MA). An example of the intercept output from the automated application is shown in Figure 5.3.

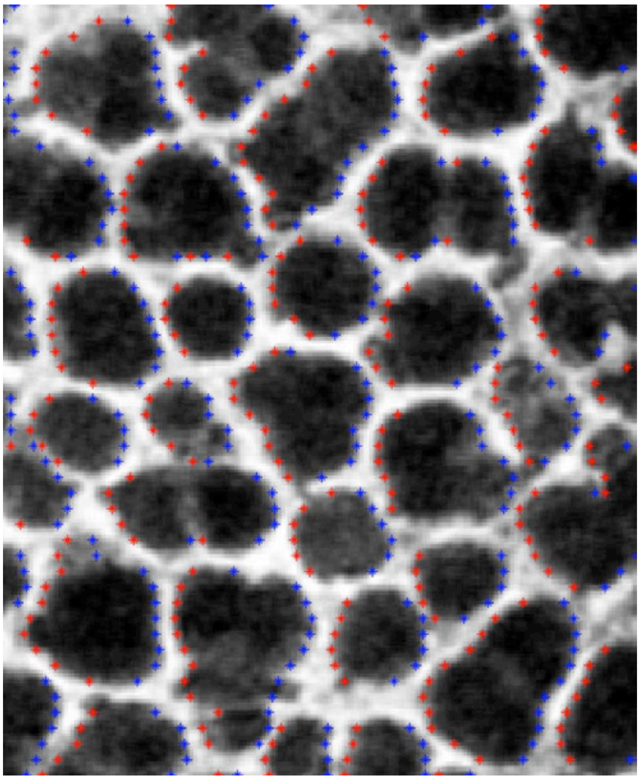

Figure 5.3: Example of automated intercept labeling. Beginning of a wall is represented by a blue cross and end of a wall by a red cross. Logging of intercepts allows accurate calculation of airspace and wall chord lengths.

The location of the beginning (blue cross) and end (red cross) of each wall intercept is displayed and logged in order to compile data on the airspace and wall chord metrics. Figure 5.6 (a) and Figure 5.7 (a) represent the final processed images for one study where intercepts have been determined using our automated analysis package. The Mean Chord Length of the airspace (MCLa) and wall (MCLw) is calculated using the following formulas

$$MCLa = \frac{\sum_{i=1}^{n} CLairS_i}{n}, \quad CLairS = \{ s \in CLair \mid s > 6 \wedge s < 120 \}, \qquad 5.1$$

$$MCLw = \frac{\sum_{i=1}^{n} CLwallS_i}{n}, \quad CLwallS = \{ s \in CLwall \mid s > 2.5 \wedge s < 35 \}, \qquad 5.2$$

where *CLair* and *CLwall* represent the chord length for the airspace and walls, respectively, and CLairS and CLwallS represent their subsets which fall within a specified range. Airspace chord lengths less than 6µm and greater than 120µm, and wall chord lengths less than 2.5µm and greater than 35µm were excluded from the mean calculation as depicted by the limits imposed on the subsets in equation 1 & 2. The lower limit of 6µm for the airspace was chosen to reduce the influence of macrophages within the airspace and red blood cells between the walls, as cross sections of either result in dark patches similar to airspaces. The upper limit of 120µm was chosen empirically; very few chord lengths surpassed this value. The lower limit of 2.5µm for the wall chord lengths was chosen to remove the effects of spurious noise, and the upper limit of 35µm was chosen again based on empirical data. Figure 5.6 (c) and Figure 5.7 (c) represent the histogram of the raw airspace chord lengths for both the inflation and deflation series, respectively. The red line indicates the median value for each distribution while γ_1 and γ_2 represent the skew and kurtosis values, respectively.

The airspace size and number are calculated using a series of image processing steps. An illumination correction based on equalizing the local mean and variance is initially applied to each confocal image. A threshold is then applied based on an optimal iterative separation algorithm [189]. The binary image is then labeled based on an 8-connected object model resulting in the segmentation of the airspace regions. Regions less than 70µm^2 were considered noise since they represent circular objects smaller than 10µm in diameter and were therefore removed. Finally, areas touching the border were also excluded. In Figure 5.6 (b) and Figure 5.7 (b), each airspace area has been identified and color-coded, where blue represents the largest (~4000 µ^2) and red represents the smallest (~400 µ^2) airspace areas.

5.2.3 Results

LSCM images of freshly excised mouse lungs (n=5) inflated to 0, 5, 10, 15, 20, 25, 30, and 35 cmH_2O pressures and then deflated in the reverse step wise order were acquired. Figure 5.4 (a-o) illustrates LSCM cross-sections at 25µm depth below the pleural surface from the same mouse lung through the inflation and deflation sequence. Images at each pressure were used for morphological analysis of mean alveolar air space chord length, mean wall chord length and total number of alveolar air spaces per field of view (FOV). In Figure 5.5 (a), the change in lung volume vs. pressure curve (static P/V loop) exhibits a hysterisis between the inflation and deflation limb which does not close, a result of the first breath phenomenon. During inflation, the number of alveolar air spaces in a given FOV vs. pressure exhibits a 'u' shape curve (Figure 5.5 (b)) where initially the number of alveolar air spaces in a FOV decreases, stabilizes at ~25 cmH_2O, and is followed by an increase in alveolar air space number as the pressure exceeds 30 cmH_2O. At the same time, mean alveolar airspace chord length (Figure 5.5 (c)) increases during inflation linearly from 5-20 cmH_2O and begins to stabilize at 20-25 cmH_2O; as the inflation pressure increases above 25 cmH_2O, the alveolar air space size remarkably begins to decrease. Also, in Figure 5.6 (c) and Figure 5.7 (c), the chord length histograms reveal a shift from smaller airspace chord lengths at lower inflation pressures to a mix of small to large chord lengths (at least two groups) at mid inflation pressures and ultimately a consolidation and shift towards small to medium sized chord lengths at the higher pressures. This phenomenon is also evident in the color-coded alveolar areas in Figure 5.6 (b) and Figure 5.7 (b). The dramatic and counter-intuitive demonstration of alveolar air space size reduction and increase in number at higher inflation pressures is direct evidence of alveolar recruitment.

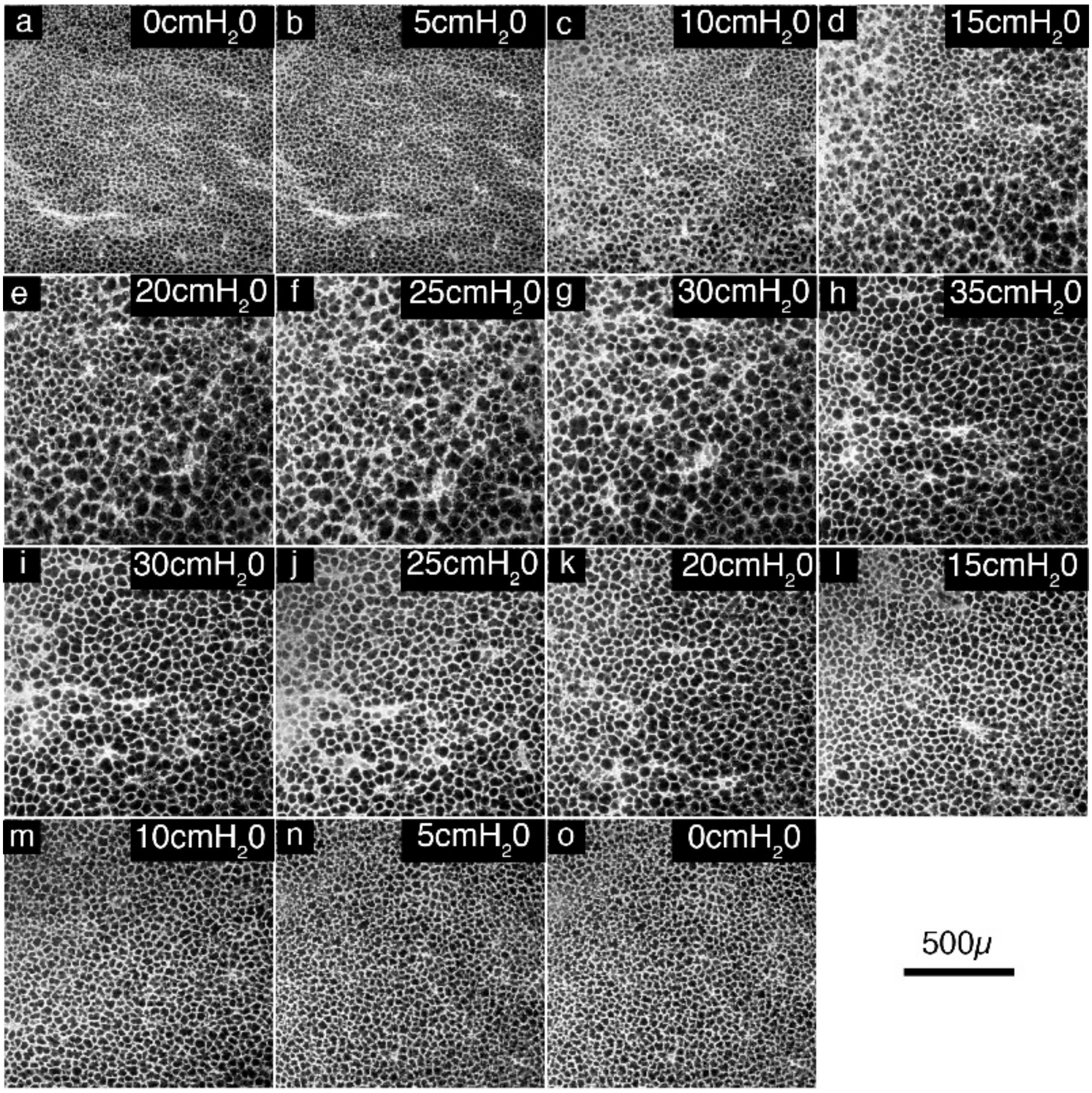

Figure 5.4: Confocal images of the same mouse lung throughout an inflation/deflation cycle. (a)-(h) represent 5 micron thick LSCM sections from the same mouse lung inflated through pressures 0-35 cmH_2O in 5 cmH_2O increments, respectively, and (j)-(o) for deflation. All images were acquired using a 10x objective and field of view of 1.2mmx1.2mm.

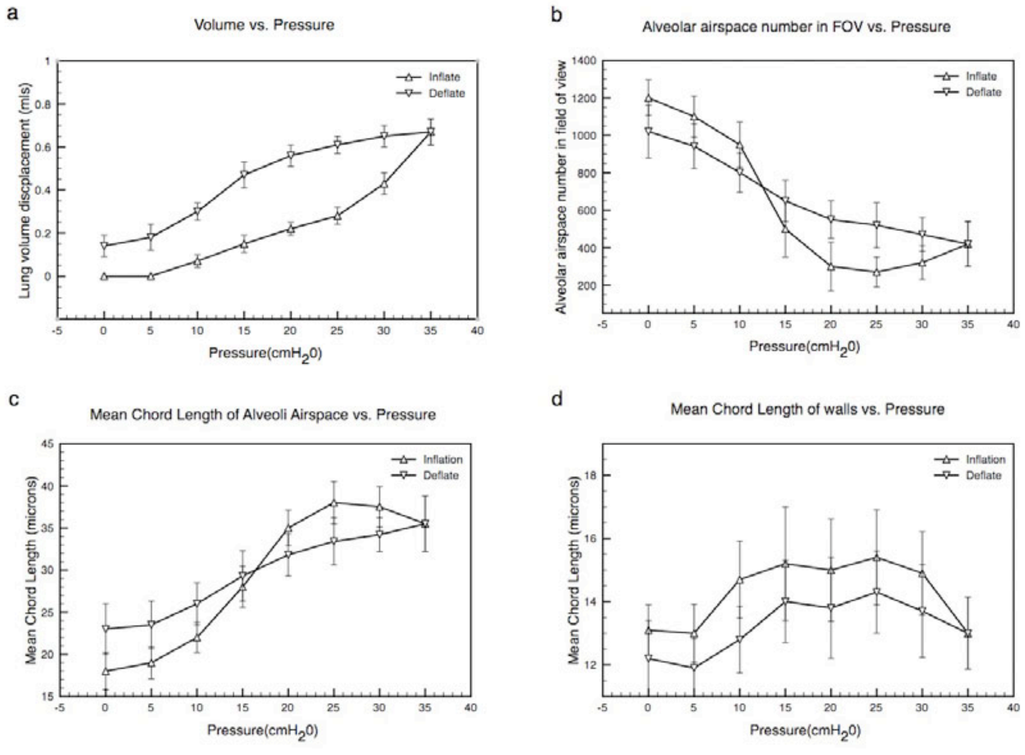

Figure 5.5: (a) Change in lung volume vs. pressure, (b) Alveolar airspace number in field of view (1.44mm2) vs. inflation pressure, (c) Mean Chord Length of alveolar airspace vs. inflation pressure, (d) Mean Chord Length of alveolar walls. Error bars represent the standard deviation (+-SD) for five mice.

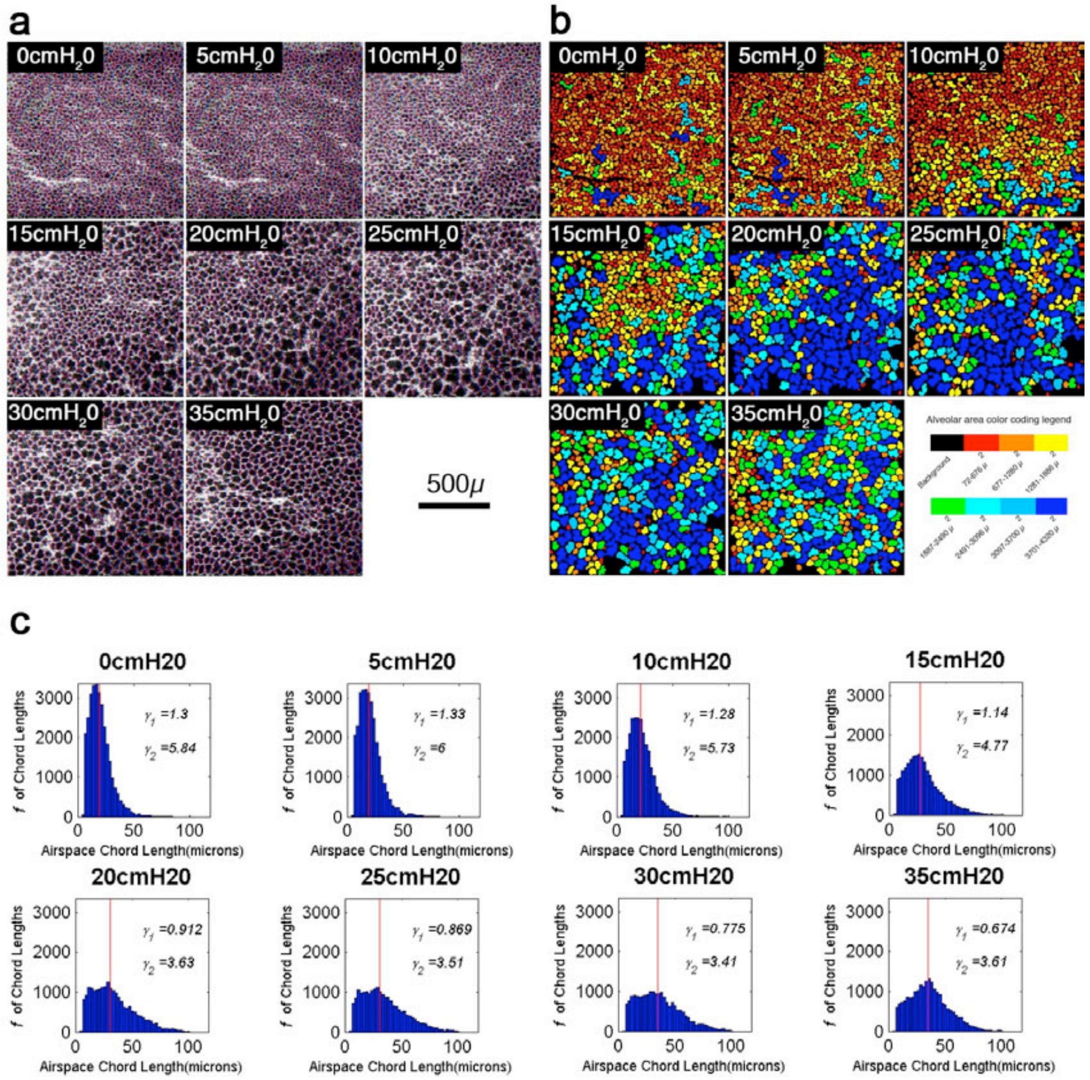

Figure 5.6: (a) Inflation 0-35 cmH_2O, with wall intercepts. (b) Inflation 0-35 cmH_2O, clustered by color-coded area (μ^2). (c) Inflation 0-35 cmH_2O, histogram of airspace chord lengths (μ). γ_1=Skew, γ_2=Kurtosis, red line = median value.

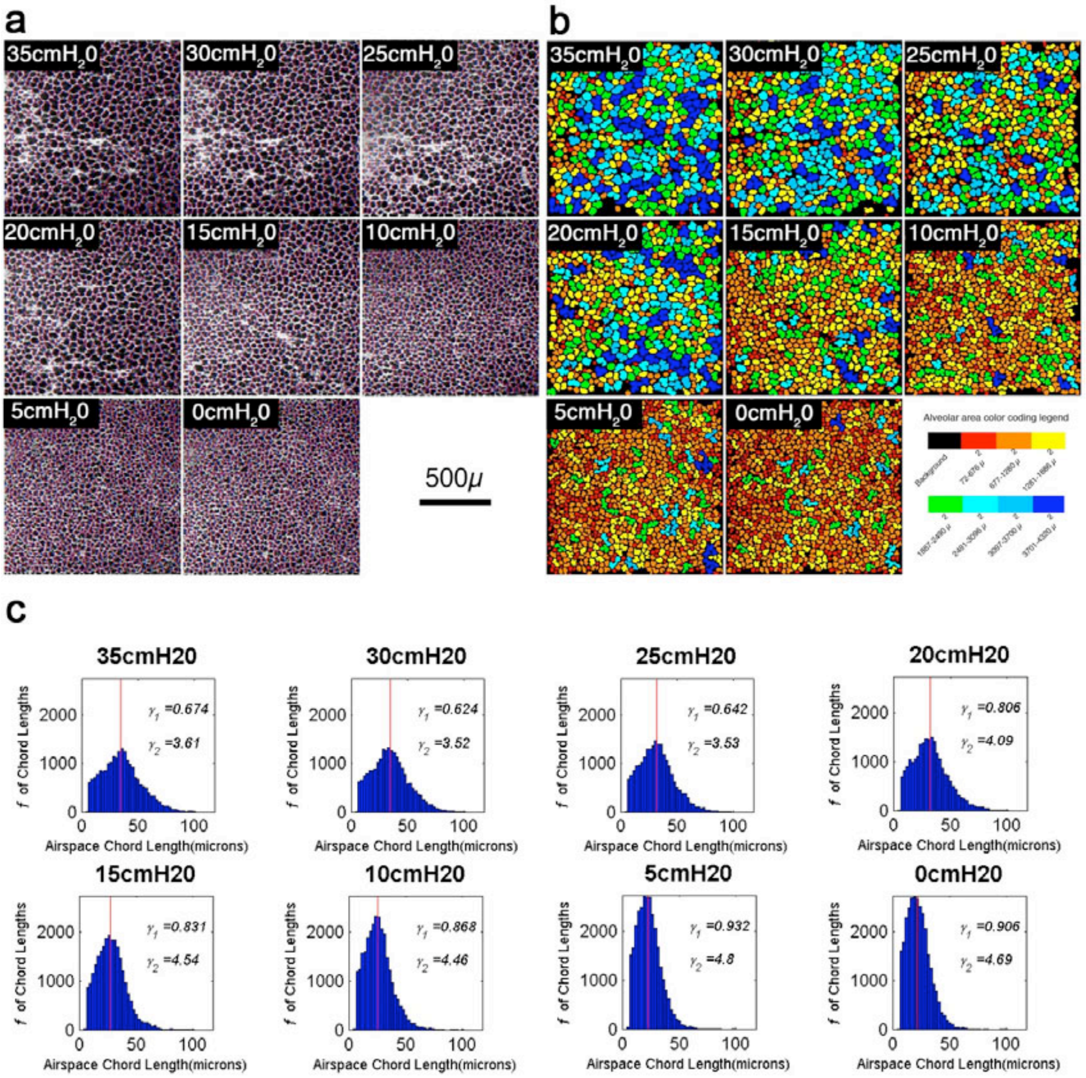

Figure 5.7: (a) Deflation 35-0 cmH_2O, with wall intercepts. (b) Deflation 35-0 cmH_2O, clustered by color-coded area (μ^2). (c) Deflation 35-0 cmH_2O, histogram of wall chord lengths (μ). γ_1=Skew, γ_2=Kurtosis, red line = median value.

5.2.4 Discussion

The laser scanning confocal technique outlined in this section presents a new opportunity to visualize the lung without fixation artifacts using optical cross sectioning capabilities. Although the technique is limited by the depth of imaging (~30 microns) due predominantly to the scattering of light at the air / tissue interface, the high resolution cross-sectional view of the alveoli provides a clearer depiction of alveolar size, shape, and number during respiration. Additionally, with vital fluorescent stains, cellular events can be imaged in 3D and 4D.

In order to counter-act or reduce the compression of the lung surface at the cover slip interface due to buoyancy, the lung has been tethered to the imaging chamber from the side via the trachea. Three-dimensional reconstructions of the sub-pleural alveoli at 10 cmH_2O and 35 cmH_2O have been made as seen in the supplementary Figure 5.8 and reveal minimal compression of the alveolar structure at the pleural interface.

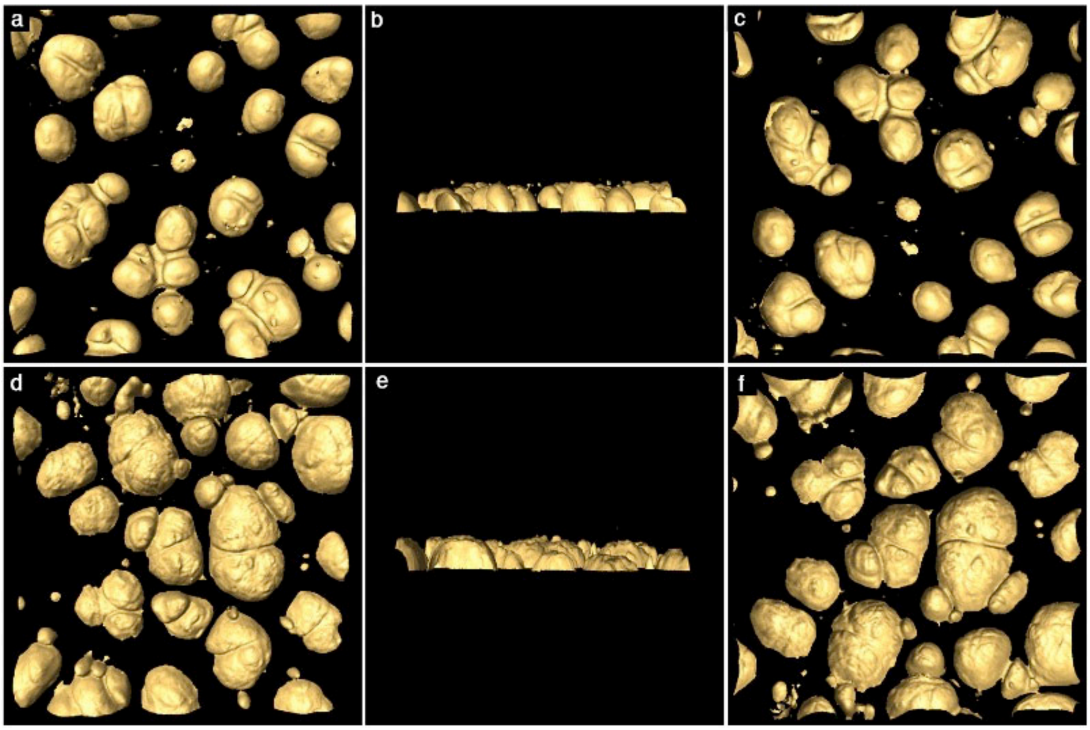

Figure 5.8: 3D comparison of sub-pleural alveoli at 10 cmH_2O (top row) and 35 cmH_2O (bottom row) airway pressure. Here, it can be seen that there is minimal compression artifacts at the cover slip interface, where (a) & (d) are looking into the lung through the pleura, (b) & (e) are side views and finally (c) & (f) are looking out of the lung through the parenchyma.

The qualitative and quantitative results presented demonstrate in the mouse lung that during an inspiration the mean alveolar size progressively increases then decreases. Simultaneously, there is a decrease followed by an increase in alveolar air space number per FOV with a similar trend reflected in the alveolar wall thickness. These results are best explained by recruitment of alveoli during high inflation pressures (similar to results presented in Lum et al [187]), since there is an increase in alveoli number (Figure 5.5 (b)) while mean alveoli airspace size is decreasing (Figure 5.5 (c)). Simultaneously, the lung volume more than doubles during the change in inflation from 25-35 cmH_2O pressure (Figure 5.5 (a)). The results are examined further in Figure 5.6 (b) and Figure 5.7 (b) where the alveoli from the same mouse lung through an inflation and deflation cycle have been color-coded against airspace size. It can clearly be seen that the change in size is not homogenous. From Figure 5.6 (c) where the distribution of the airspace chord lengths has been plotted, the skew (γ_1) and median value depicted by the red line is shifting towards a normal distribution ($\gamma_1 \rightarrow 0$). Simultaneously, the kurtosis (γ_2) is shifting from a leptokurtic (small tail) distribution towards a platykurtic (large tail) distribution. This reveals an increase in heterogeneity of the chord lengths through the inflation phase. Also, Figure 5.6 (b) demonstrates that during the higher inspiratory pressures the alveoli are becoming smaller, again evident from the shift in chord length distribution and the median value towards the left seen in Figure 5.6 (c). Detection of smaller alveoli during inflation is in agreement with a previous study by Smaldone et al. [186], and the increase in the number of alveoli is also in agreement with studies perfomed by Escolar et al. [188]. Our results also show high heterogeneity between alveoli during inflation; this agrees in part with a previous study that had proposed three types of alveoli: those that do not change with inflation, those that do change, and those that collapse at the end of inspiration [182].

At the end of this first inflation / deflation maneuver, the mean alveolar airspace has increased as evident by the color-coded images in Figure 5.6 (b) and Figure 5.7 (b). The distribution of the airspace chord lengths in Figure 5.6 (c) and Figure 5.7 (c) also reflects this increase where the distribution is less skewed at the end of deflation (0 cmH_2O) when compared to the initial inflation image (0 cmH_2O). The lung volume is also greater at the end of the maneuver as evident in Figure 5.5 (a), suggesting recruitment. It is quite remarkable that alveoli become smaller and more numerous at pressure gradients greater than 25 cmH_2O, as pressure levels of 15-25 cmH_2O should be sufficient for the majority of recruitment to occur. A complex mechanism that recruits large numbers of alveoli at high inflation pressures seems to exist.

To explain these findings, we propose a mechanism in which there exist main or mother alveoli that directly connect to the conducting airways, and daughter alveoli, that connect to the mother alveoli, recruited via the pores of Kohn. During inflation up to 25cm H_2O as the alveolar size increases and the walls stretch, we propose that the diameter of the pores of Kohn also increases, leading to a thinning of the surfactant layer that has been shown to normally cover the pores of Kohn [19]. When the pressure gradient between the mother and daughter alveoli becomes greater than that which the thinning surfactant layer over the pores of Kohn can withstand, air passes into the daughter alveoli, which are then recruited. Until this set of conditions is met, the pathways to recruiting the daughter alveoli are closed. We propose during deflation the pressure reduces in the mother and daughter alveoli simultaneously until the pores of Kohn reduce in diameter and the surfactant layer reforms its seal, trapping the remaining air inside the daughter alveoli. This process would then be stepwise or irregular during inflation and smooth or linear during deflation, in agreement with the empirical data obtained here.

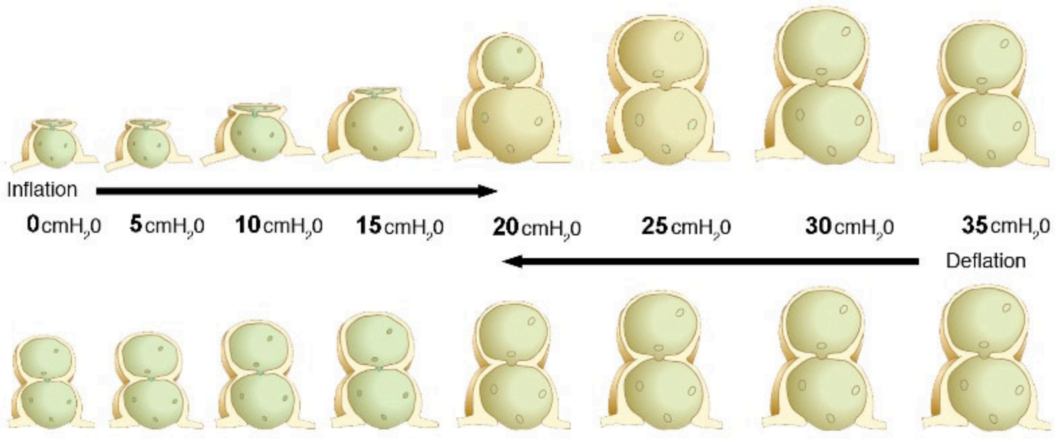

Figure 5.9: Cartoon depiction of the mother/daughter alveolar hypothesis during the first breath post deflation. During inflation, the mother alveoli incrementally expand with proportional expansion in the alveolar walls and pores of Kohn. As the surfactant layer over the pores of Kohn becomes thinner and the pressure gradient between the mother and daughter alveoli increases, air passes through to the daughter alveoli. The recruitment of the daughter alveoli leads to a subsequent reduction in the average size of the mother alveoli as more lung volume is distributed. During deflation, the pressure reduces in both the mother and daughter alveoli until the pores of Kohn reduce in diameter and the surfactant layer reforms its seal, trapping the remaining air inside the daughter alveoli and leading to recruitment of the daughter alveoli. Note: pressure values have been extrapolated from the empirical data obtained in the present mouse lung study.

The suggested hypothesis is illustrated in Figure 5.9. For the sake of simplicity, we have depicted a single daughter alveoli per mother alveoli, however this hypothesis is not limited to such a case. Rather, some may have no daughter alveoli, while in other circumstances, several daughter alveoli may be connected to one mother alveoli. In such situations, the daughter alveoli would also become a communicating pathway between groups of adjacent mother alveoli. Current understanding of lung anatomy indicate ventilatory units within an acinus consisting of the alveolar duct and subtended alveoli [190]. Stacking these structures into an organ against a boundary, such as the pleura, means that these structures cannot occupy all of the space. Alveoli that are air filled directly from other alveoli could fill this space, as illustrated in Figure 5.9.

Subsequent breaths would then behave differently than a breath taken from passive deflation; this needs further investigation. If all alveoli were connected to a branching airway, a long standing hypothesis supported by anatomical studies, they should all inflate uniformly unless their compliance were some how different, or they had a mechanism for closure of their mouth to prevent airflow. As seen in this study and those reviewed in Gatto et al [185], the alveoli are not isotropically expanding; there is a complex process combining expansion and contraction of alveoli, recruitment and de-recruitment as well as static alveoli throughout the respiratory cycle.

Surfactant integrity would clearly play a pivotal role in this mechanism for recruitment / de-recruitment of alveoli, consistent with previous studies where instability of alveoli was linked to the integrity of the surfactant [14, 182-184]. The results of a recently presented study indicate that alveolar instability is greater with low PEEP (5 cmH_2O) and high tidal volume, while alveolar stability can be achieved with high PEEP (20 cmH_2O) and low tidal volume [179]. This observation is also consistent with the mother/daughter hypothesis where at low PEEP and high tidal volume, the pores of Kohn would be continuously opening and closing during inspiration and expiration, leading to instability as a result of the increase in recruitment / de-recruitment (i.e. increase in mechanical stress). With the high PEEP and low tidal volume, the pores of Kohn would remain open during inspiration and expiration, which would maintain recruitment and decrease the likelihood of de-recruitment leading to overall stability of the alveoli. The heterogeneity of the recruitment process could also be linked to the previously observed heterogeneous number and regional distribution of the pores of Kohn [191].

The mother daughter hypothesis also makes sense if we think about the structural benefit of having such daughter alveoli, which are recruited only at high pressures, a time when the stress on the already inflated alveoli would be extremely high [192]. With the recruitment of the daughter alveoli and subsequent reduction in the average size of the mother alveoli as more lung volume is distributed, the tension in all interconnected walls would be reduced. The results presented with the hypothesis could also lead us to better understand why mice have an irregular double humped inflation curve, a long-standing mouse lung physiology question {Soutiere, 2004 #217}.

The pores of Kohn in the hypothesis would not only facilitate alveolar recruitment, but would also be available for collateral ventilation at high lung volumes, as seen at deep inspiration and in diseases associated with lung over inflation such as pulmonary emphysema.

Current fixation and evaluation of lung morphology through two-dimensional histopathology can not easily demonstrate mother/daughter alveoli, since the process of fluid filled fixatives in the airways would result in the expansion of both the mother and daughter alveoli without the need for high pressure gradients as seen in saline filled lungs. Although vascular perfusion following labor-intensive serial sectioning at various points along the pressure-volume curve have and can provide greater insight into the three-dimensional mechanics of the alveoli [193], more sophisticated microscopy techniques are still needed to produce further anatomical evidence of the proposed hypothesis.

From this study, we can draw several conclusions. In a deflated lung undergoing inflation, the alveoli are initially unstable. After one inflation / deflation maneuver, both the lung volume and mean alveolar airspace increases. The increase in open / recruited alveoli increases the stability of the lung. From this, we hypothesize that subsequent cycles would progressively increase the stability of the alveoli until eventually the majority become stable and exhibit minimal change in size during tidal breathing as postulated by groups of Radford et al. [194] and shown in Nieman et al. [14, 170, 179, 181-184, 195-198] and Escolar et al. [188].

The mother daughter alveoli hypothesis, arising from direct observation and measurement of the sub-pleural alveolar environment in fresh intact mouse lungs, is a reasonable explanation of the empirical data obtained in this study. Although there is no firm proof that anatomically the daughter alveoli exist, there is also equally no firm evidence that they do not exist.

5.2.5 Conclusion

In this section, we describe an *ex vivo* LSCM imaging technique to image intact fresh mouse lungs. A study using this technique is presented, which assesses alveolar morphology over a respiratory cycle in five mice lungs. For the first time, high-resolution cross-sectional images of the alveoli were obtained over sequential inflation and deflation pressures within the same lung. Automated imaging algorithms were developed to extract alveolar metrics from these images, and quantitative results confirmed for the first time direct evidence of alveolar recruitment, a long-standing question in lung structure and function. From the empirical results found in this study, a new theory on alveolar mechanics was proposed.

5.3 In Vivo Lung Imaging

5.3.1 Introduction

Understanding the structure and function of alveoli *in vivo* is crucial for understanding the normal and diseased lung. The question of alveolar size and number change during the full breathing cycle remains incomplete, yet is fundamental for understanding alveolar based diseases [173, 184, 188]. Repeated quantitative visualization at the alveolar level in unfixed breathing lung, without the overlying pleura partially obstructing the view, has only recently been achieved as described in Section 5.2.

Respiratory diseases, such as emphysema where there is an enlargement of alveoli over time, would greatly benefit from the ability to non-invasively assess alveolar degeneration. In particular, tracking of alveolar size over time to assess mechanical and pharmaceutical therapies would have a major impact.

The process of recruitment and de-recruitment of alveoli has been controversially discussed with no unifying theory on its mechanism. There are several common hypotheses not restricted to: balloon-like expansion of alveoli, limited expansion of alveoli with major expansion in airways and ducts, or continual recruitment and de-recruitment of alveoli [173]. With the *ex vivo* imaging presented in Section 5.2, we now have a greater ability to solve this question, and if we are able to image the alveoli *in vivo,* we could potentially bring new light into this well discussed theory.

In this study, we use a Catheter Based Confocal Microscope (CBCM) system to visualize alveoli of living mouse lungs and directly measure alveolar size, area and number using an automated application. Alveolar structure in the normal mouse lung as seen through standard histology seems to have an ordered and uniform structure. In this study, we show through direct means that the alveolar structure *in vivo* is highly heterogeneous and that the “popping” phenomenon, described in the earlier section of this chapter, does occur *in vivo*.

Until recently, the predominant source of information on alveolar structure and function has been through observations in histology and whole lung mechanics. Currently, there is very little known about the true three-dimensional shape of the alveoli and its dynamic behavior in the breathing lung. Gaining visual insight into an organ, which has such a vast range of functional motion (breathing), requires a new approach. In the following section, we discuss a novel technique termed catheter based confocal microscopy (CBCM), which enables *in vivo* microscopy via sub-millimeter fiber bundles.

5.3.2 Methods and Materials

5.3.2.1 Animal Preparation

Animal experiments carried out in this study were approved by the University of Iowa Animal Care Committee. Normal C57BL/6 mice aged between 6-8 weeks, weighing 19-21 grams, were used for this study. Mice were initially sedated using 3-5% isofluorane followed by an IP injection of 87.5mg/kg ketamine and 12.5mg/kg xylazine. Following a negative pedal reflex, 50mg/kg sodium fluorescein was administered IP and allowed ten minutes for uptake. A tracheotomy was performed with insertion of a 20-gauge catheter. Mice were then mechanically ventilated using a modified Columbus CIV-101. A thoracotomy was performed and the chest wall was surgically removed revealing the lung and heart. Between image acquisitions mice were ventilated at 120br/min and 0.5ml tidal volume. During imaging a 5 second breath-hold was induced at a user defined pressure level using a custom developed microcomputer pressure controller system [199]. Mice vitals were also monitored using an ECG and pulse oximetry meter. The ECG probes were attached to the paws, while the pulse oximeter sensor was attached to the tail.

5.3.2.2 Laser Scanning Confocal Imaging

A Bio-Rad 1024 Radiance confocal microscopy system configured with a Krypton-Argon 488nm laser was used for this imaging study. A custom attachment was designed and built in order to inject the light from the laser scanning Bio-Rad microscope into a coherent imaging fiber bundle. A schematic of the Bio-Rad microscope with the custom CBCM attachment is shown in Figure 5.10.

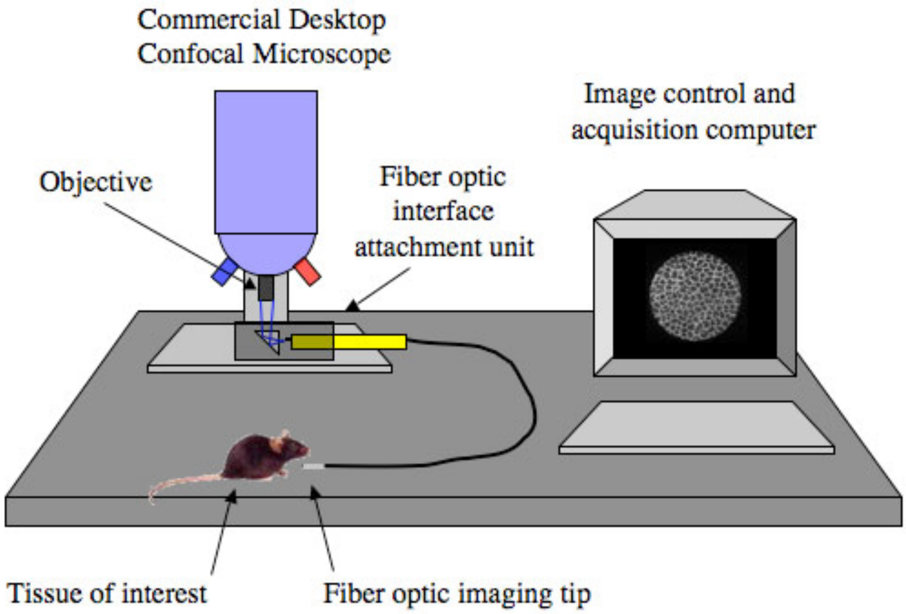

Figure 5.10: Schematic of the Catheter Based Confocal Microscope system utilizing a commercial Bio-Rad microscope and a custom fiber injection attachment.

The system incorporates a 30,000 fiber optic imaging bundle (Fujikura America Inc, GA), coupled via a custom stage attachment to a commercial Bio-Rad 1024 confocal microscope. The proximal end of the fiber bundle is scanned with a 488nm wavelength laser. The fiber bundle relays the scan to the distal end where the fiber bundle (Figure 5.11) is brought into contact with the tissue of interest. The fluorescent signal emitted from the tissue, is relayed back through the fiber, and allows for image formation at the proximal end, which is simultaneously scanned and detected by a high gain photo multiplier tube.

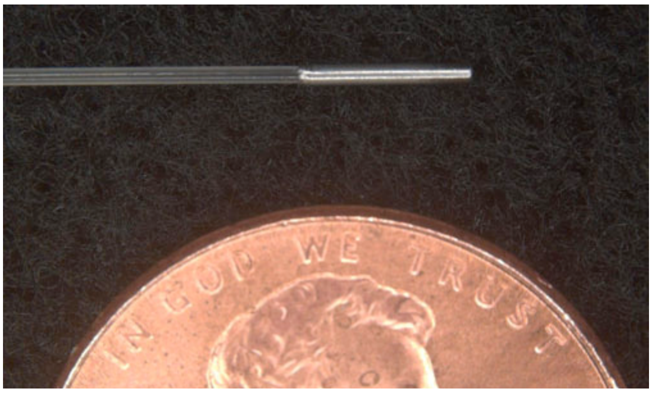

Figure 5.11: Distal end of the fiber optic catheter tip imaged against a United States penny, depicting its small size. (<0.9mm diameter).

Fluorescein (50mg/kg) was administered I.P. for general visualization of tissue structure. Acridine Orange (20µl at 100g/ml) was applied topically to allow for visualization of nuclei.

5.3.2.3 Image Processing

Prior to the image analysis, there are several automated pre-processing steps, which are undertaken in order to increase the accuracy of the analysis system. The CBCM images acquired through the imaging bundle have a distinct fiber pattern as seen in the zoomed raw fiber image shown in Figure 5.12.

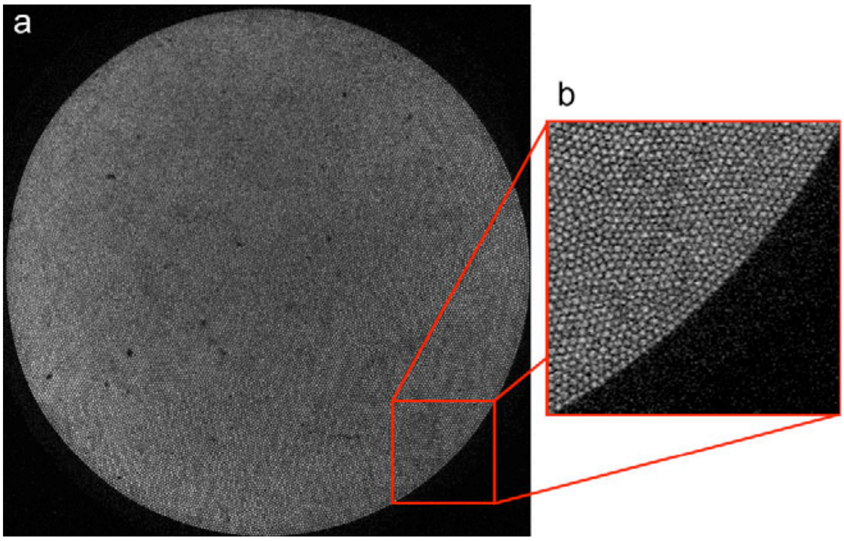

Figure 5.12: (a) CBCM raw fiber image and (b) zoomed region shown in the red box. Note the fiber pattern is clearly apparent.

This pattern is considered noise and is initially removed prior to analysis. A flow diagram of the processing steps used to remove and smooth the image is shown in Figure 5.13.

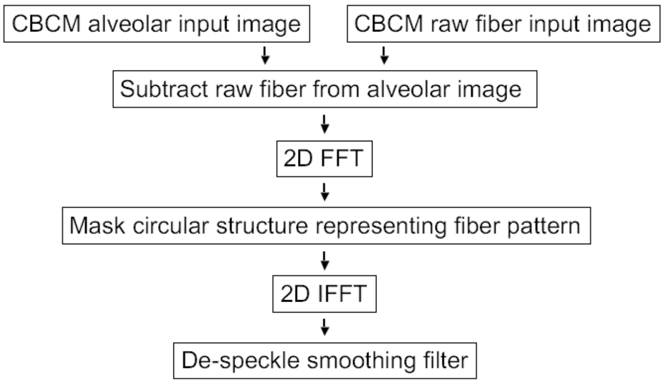

Figure 5.13: Image processing flow diagram for filtering CBCM images of alveolar structure.

Initially a background image is acquired where fiber locations along with fiber bundle polishing artifacts can be identified. This background image is then subtracted from every future acquired frame, as shown in Figure 5.14 (a). This predominantly reduces noise due to imperfections on the proximal and distal surfaces of the imaging bundle, which remain constant during image acquisition.

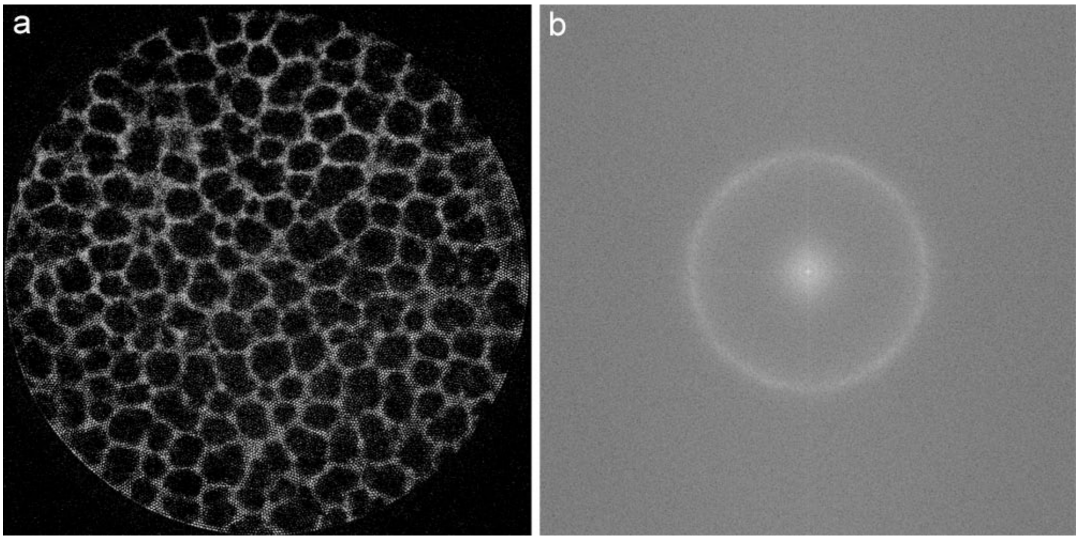

Figure 5.14: (a) raw fiber subtracted CBCM image of alveolar structure and (b) two-dimensional FFT of (a).

A 2D Fast Fourier Transform (FFT) is then performed on this image, as shown in Figure 5.14 (b). Here, we can identify a ring structure that correlates to the fiber pattern from the imaging bundle. A mask is created and applied to remove the ring structure in the FFT image, and an inverse 2D Fast Fourier Transform (IFFT) is calculated producing an image where the fiber pattern has been filtered. Finally, a smoothing filter is applied to reduce the speckle noise. The original and the final filtered image are shown in Figure 5.15 (a) and (b), respectively.

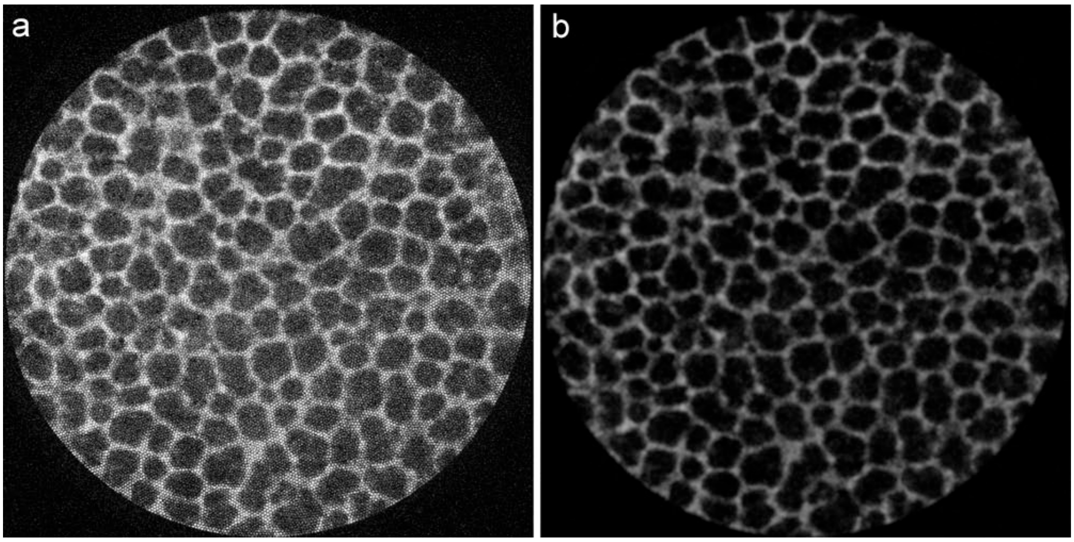

Figure 5.15: (a) original CBCM image of the alveolar structure and (b) the final filtered image.

5.3.2.4 Image analysis

The mean chord length (MCLa) of the alveolar airspace, a common lung metric [200, 201], along with mean chord length of the alveolar walls (MCLw) and alveolar airspace number are calculated using an automated application developed using Matlab (Mathworks, Natick MA) and described in Section 5.2.2.6. Slight modifications were made to the program, detailed in Section 5.2.2.6, in order to accommodate for the disc shape region of interest (fiber optic field of view). In brief, the program determines the beginning and end of alveolar walls along specified parallel lines in an automated fashion as commonly performed in lung morphology. This enables calculation of both the mean chord length of alveolar airspace (MCLa) and mean chord length of alveolar walls (MCLw). The Mean Chord Lengths are calculated using the following formulas

$$MCLa = \frac{\sum_{i=1}^{n} CLairS_i}{n}, \quad CLairS = \{ s \in CLair \mid s > 6 \wedge s < 120 \}, \tag{5.3}$$

$$MCLw = \frac{\sum_{i=1}^{n} CLwallS_i}{n}, \quad CLwallS = \{ s \in CLwall \mid s > 2.5 \wedge s < 35 \}, \tag{5.4}$$

where CLair and CLwall represent the chord length for the airspace and walls, respectively, and CLairS and CLwallS represent their subsets which fall within a specified range. Airspace chord lengths less than 6µm and greater than 120µm, and wall chord lengths less than 2.5µm and greater than 35µm are excluded from the mean calculation as depicted by the limits imposed on the subsets in equation 5.3 & 5.4. The lower limit of 6µm for the airspace was chosen to reduce the influence of macrophages within the airspace and red blood cells between the walls, as cross sections of either result in dark patches similar to airspaces. The upper limit of 120µm was chosen empirically as very few chord lengths surpassed this value. The lower limit of 2.5µm for the wall chord lengths was chosen to remove the effects of spurious noise, and the upper limit of 35µm was chosen again based on empirical data. An example of the intercept output from an in vivo image analyzed using the automated application is shown in Figure 5.16, where the blue and red crosses represent the beginning and end of a detected wall, respectively.

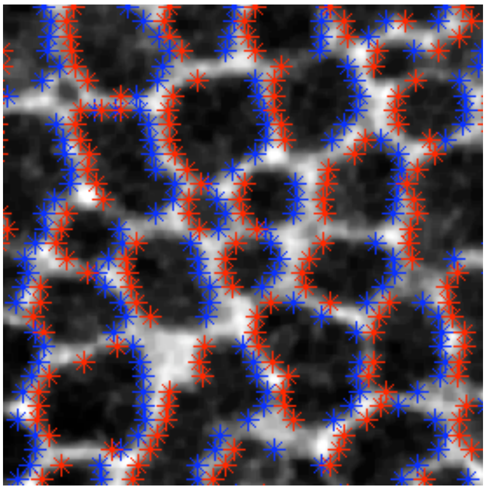

Figure 5.16: In vivo laser scanning confocal microscopy of alveolar walls with automated wall intercept analysis overlaid.

The airspace size and number is calculated using a series of image processing steps as outlined in Figure 5.17.

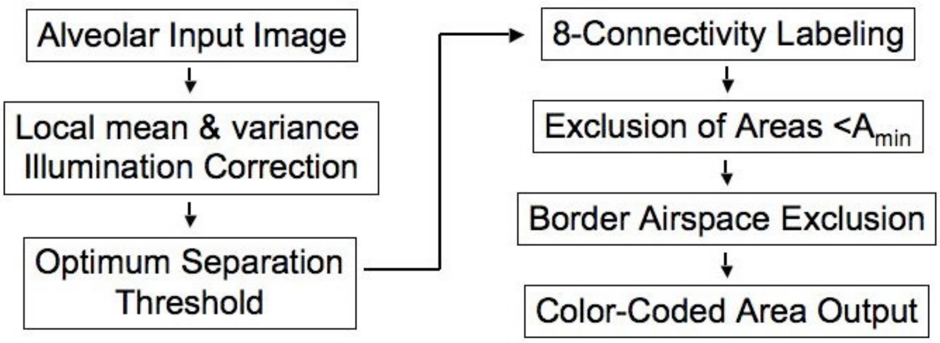

Figure 5.17: Outline of image processing steps for calculating alveolar airspace number and size.

An illumination correction based on equalizing the local mean and variance is initially applied to each confocal image. This is especially important in the CBCM image acquisition system since it is essentially a surface scanning technique where slight deviations in the surface angle of the fiber probe and the tissue of interest can have a dramatic effect on image contrast. A threshold is then applied based on an optimal iterative separation algorithm [189]. The binary image is then labeled based on an 8-connected object model resulting in the segmentation of the airspace regions. Regions less than Amin = 70µm^2 are considered noise since they represent circular objects smaller than 10µm in diameter and are therefore removed. Finally, areas touching the border are also excluded.

5.3.3 Results

5.3.3.1 Alveolar Airspace Analysis

During a 25 cmH_2O pressure breath-hold, images were acquired through the pleura of anesthetized and ventilated mouse lungs. Using the general sodium fluorescein staining, as detailed in Section 5.3.2.2, clear depiction of the alveolar walls and airspace can be seen in Figure 5.18. Using the topically applied Acridine Orange dye, the nuclei can be visualized as seen in Figure 5.19.

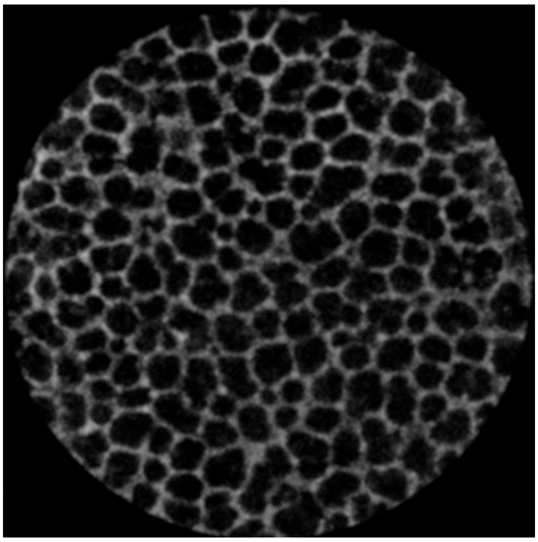

Figure 5.18: In vivo catheter based laser scanning confocal microscopy of alveolar walls – Fluorescein dye.

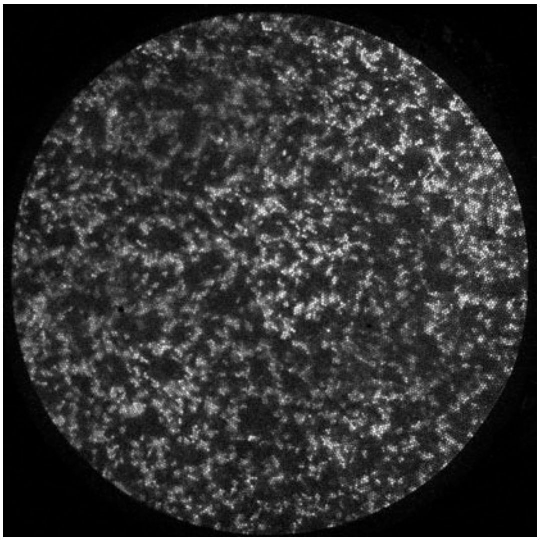

Figure 5.19: In vivo catheter based laser scanning confocal microscopy of nuclei – Acridine Orange dye.

Figure 5.18 has been analyzed as detailed in Section 2.4 for airspace and wall chord metrics, as shown in Figure 5.20 (a) where the MCLa was calculated as 39µm and the MCLw was calculated as 12µm.

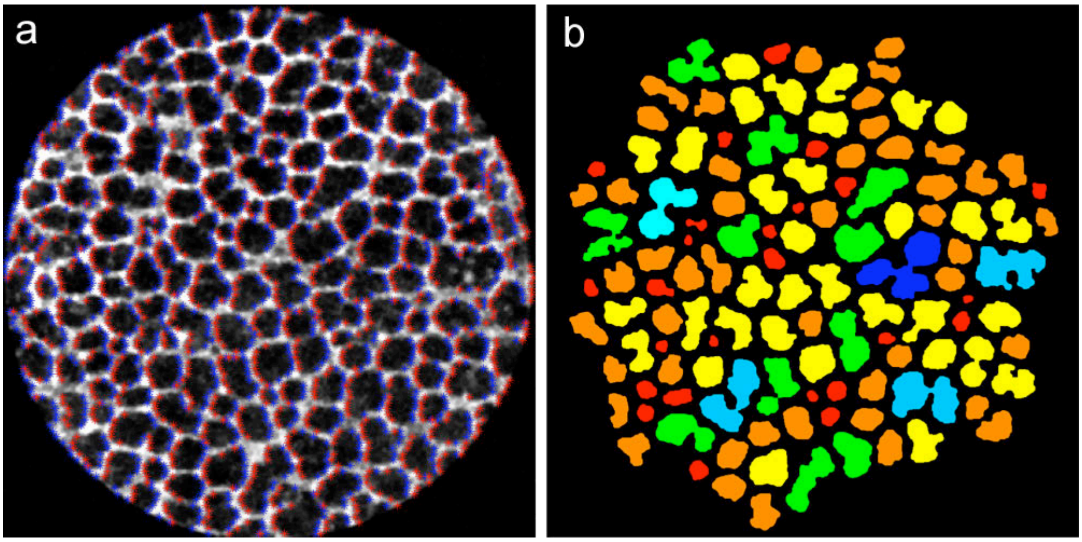

Figure 5.20: (a) airspace and wall chord analysis on CBCM alveolar image shown in Figure 5.18. The calculated MCLa is 39µm and the MCLw is 12µm. (b) area based cluster analysis of CBCM alveolar airspace, where 121 spaces have been identified from small (red) to large (dark-blue).

The airspace number and area were also calculated, as detailed in Section 5.3.2.4 and shown in Figure 5.20 (b) where 121 alveolar airspaces have been identified in this particular example. In Figure 5.20 (b), each airspace area is color-coded, where blue represents the largest (~6000 µ2) and red represents the smallest (~400 µ2) airspace areas.

Currently, this informative analysis sequence is performed offline requiring less than 60 seconds of computation for a 1024x1024 pixel image on a standard PC. In future, both the filtering and analysis steps will be performed on high-end CPU and GPU processors, enabling real-time analysis of alveolar area, size and number during image acquisition.

5.3.3.2 Alveolar Recruitment Example

Using a commercial high-speed catheter-based confocal microscope (CBCM) system (Cellvizio, Mauna Kea Technologies, France) similar to the one described above, the alveolar recruitment hypothesis presented in Section 5.2.4 has been investigated on lungs of live mice.

Images were acquired using the Cellvizio CBCM system on C57BL/6 mice expressing Green Fluorescent Protein (GFP) for endogenous fluorescent visualization of the lung parenchyma. Figure 5.21 represents two examples using this technique through the mouse lung pleura. Here, a series of sequential images was acquired over 250ms. In both examples, we can clearly observe the “popping” open and recruitment of an alveolus as indicated by the red arrows. A video of both sequences has also been included in Appendix D the “Supplementary Data CD”.

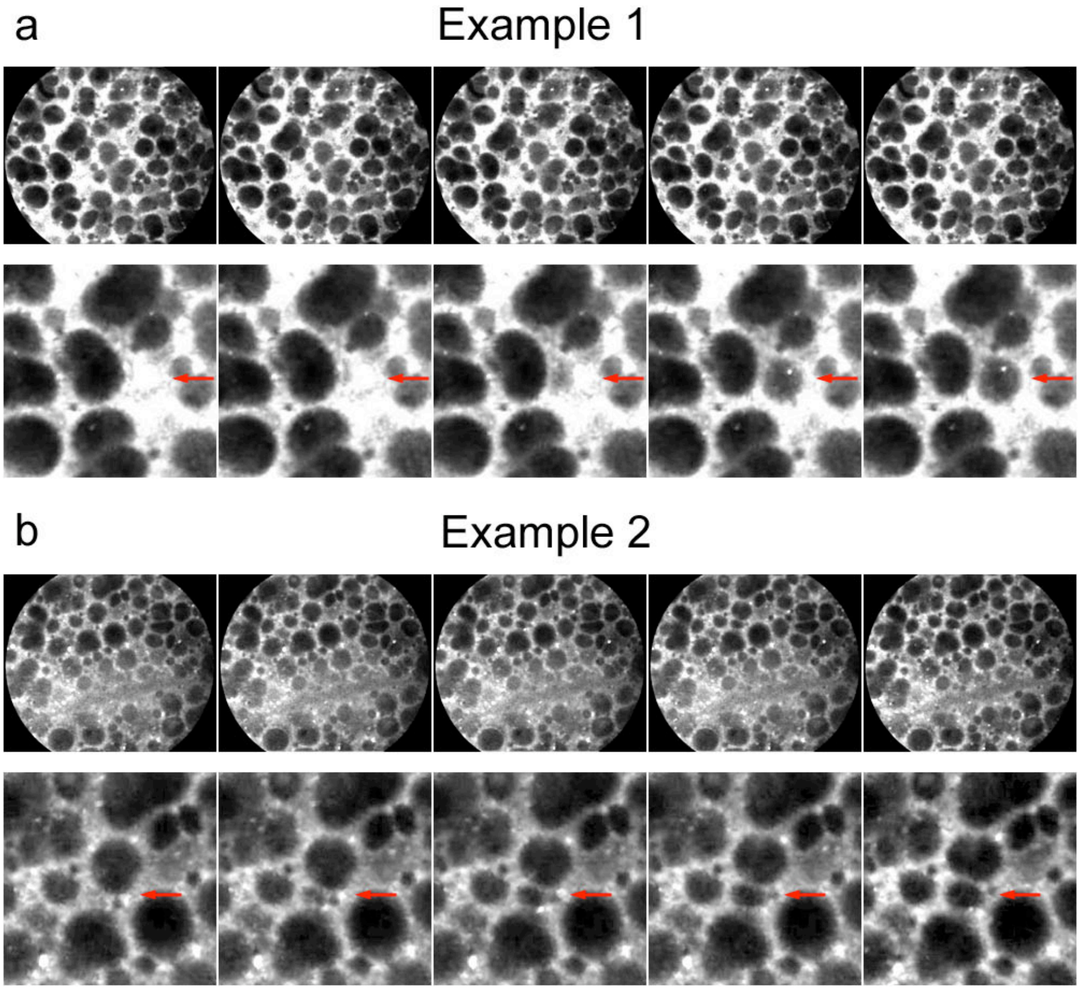

Figure 5.21: Two examples of alveoli ‘popping’ open in C57BL/6 mice lungs expressing GFP. Each frame was captured over 50ms. Acquired using a catheter-based confocal microscopy technique.

5.3.4 Discussion

The *in vivo* imaging results confirm that direct dynamic visualization of alveoli and surrounding structures is possible. Furthermore, analysis of the alveolar area, size and number has been accomplished using this imaging approach; with further development, the potential for real-time analysis is viable.

From the analysis example, it is evident that there is high heterogeneity in the sub-pleural alveolar airspace *in vivo*. It is interesting to note that, although there is a heterogenic distribution of alveolar sizes, there does seem to be an underlying pattern. This pattern is best described by the even spread of small alveoli, as seen in the area based analysis in Figure 5.20 (b) represented by the red regions. Equally larger alveolar spaces as seen from the orange, yellow and green regions also seem to follow this uniform spread, but in higher proportions. At this stage, the underlying reason for this pattern is unknown and is currently under investigation.

With the limited acquisition speed of commercial desktop confocal microscopes (<5fps), a high-speed commercial CBCM system was needed and utilized for investigation of the alveolar recruitment phenomenon described in Section 5.2.4. Here, it was confirmed that the alveolar “popping” phenomenon occurs *in vivo* in normal mice. From the presented examples, it is also clear that when a daughter alveolus opens, the connecting mother alveolus reduces in size.

Using the presented techniques, imaging of alveoli through the sub-tending airways in the human situation becomes a reality. This has important implications for alveolar based diseases, such as emphysema where there is a great need for direct visualization of alveoli at the bedside.

5.3.5 Conclusions

We present *in vivo* alveolar imaging in mouse lungs using an optical fiber-based system. This imaging system is ultimately adaptable for *in vivo* imaging of alveoli in the human lung where direct visualization at the bedside is greatly needed.

Also presented is the automated morphologic analysis of alveoli in mouse lungs from *in vivo* CBCM images. The examples presented reveal that there is a high heterogeneity in sub-pleural alveoli imaged *in vivo*, rather than an ordered uniform structure as commonly believed.

Using the techniques presented here, there is great promise for advancing our knowledge of the important functional unit of the lung, the alveolus, for alveolar mechanics, cell traffic and 3D structural visualization.